Journal of Inorganic and General Chemistry
ZAAC
Zeitschrift für anorganische und allgemeine Chemie
www.zaac.wiley-vch.de
RESEARCH ARTICLE

DOI: 10.1002/zaac.202200133

Kinetic Stabilization of Heavier Bis(*m*-terphenyl)pnictogen Phosphaethynolates

Daniel Duvinage[+],[a] Marvin Janssen[+],[a] Enno Lork,[a] Hansjörg Grützmacher,[b] Stefan Mebs,*[c] and Jens Beckmann*[a]

Dedicated to Professor Cameron Jones on the occasion of his 60th birthday

Kinetic stabilization using bulky *m*-terphenyl substituents is the key to the isolation of the diarylantimony and diarylbismuth phosphaethynolates (2,6-$Mes_2C_6H_3)_2$EPCO and the related N-heterocyclic carbene complexes (2,6-$Mes_2C_6H_3)_2$EP(O)C(IMe_4) (E = Sb, Bi; IMe_4 = 1,3,4,5-tetramethylimidazol-2-ylidene), which have been fully characterized crystallographically and spectroscopically. The experimental characterization was augmented by a DFT based real space bond indicator analysis of the electron density, including AIM, NCI, and ELI-D methods.

Introduction

The phosphaethynolate ion, $[PCO]^-$, a heavier congener of the cyanate ion $[NCO]^-$, has proven to be a versatile building block in synthetic main group element chemistry.[1,2] In light of one of its significant resonance structures which may be written as $[P{\leftarrow}C{\equiv}O]^-$, it can be viewed as synthon for the $[P]^-$ ion, which has been used for the (photochemical) preparation of phosphinidenes and phospha-heterocycles formed upon decarbonylation. Recently developed synthetic procedures now allow the convenient preparation of the $[PCO]^-$ ion on a multi-gram scale.[3] In coordination chemistry, efforts were made to explore the ambiphilic nature of the $[PCO]^-$ ion, which may coordinate via their phosphorus or oxygen atoms giving rise to metal phosphaketenes, M–P=C=O, or their oxyphosphaalkyne analogues M–O–C≡P. While such compounds have been established where the OCP unit is bound to an element from group 13 or 14, the preparation of compounds with heavier elements from group 15 is challenging.

Very recently, Benkő and Gilliard et al. reported on the salt metathesis reaction of Na[OCP] with Ph_2SbCl and Ph_2BiCl, respectively, aimed to allow for the complexes Ph_2EPCO, but producing the tetraphenyldipnictines Ph_2EEPh_2 and ill-defined precipitates instead (E = Sb, Bi).[4] They also found that the reaction of the related N-heterocyclic carbene (NHC) complexes $Ph_2E(I^iPr_2Me_2)Cl$ with Na[OCP] proceeded with NaCl elimination without yielding the desired metathesis products $Ph_2E(I^iPr_2Me_2)PCO$ (E = Sb, Bi; $I^iPr_2Me_2$ = 1,3-diisopropyl-4,5-dimethylimidazol-2-ylidene), which might have formed only as transient intermediate that rapidly rearrange into complexes $Ph_2EP(O)C(I^iPr_2Me_2)$ having the same elemental composition (Scheme 1). The rearrangement may be rationalized by the migration of the NHC from the pnictogen atom to the carbon atom of the PCO moiety, for which a mechanism was proposed on the basis of density function theory (DFT). Although fully characterized, the complexes $Ph_2EP(O)C(I^iPr_2Me_2)$ turned out to be metastable with respect to the formation of the tetraphenyldipnictines Ph_2EEPh_2 and the salt $[(I^iPr_2Me_2)PC(O)(I^iPr_2Me_2)][PCO]$, as slow decomposition was observed even at −37 °C in the solid state (Scheme 1). The formation of the tetraphenyldipnictines Ph_2EEPh_2 might have been facilitated by the secondary pnictogen-pnictogen interactions evident in the crystal structures of $Ph_2EP(O)C(I^iPr_2Me_2)$.

In this work, we addressed the stability issues Benkő and Gilliard et al.[4] were facing in their work, using bulky *m*-terphenyl substituents providing sufficient kinetic stabilization not only to the NHC-supported complexes (2,6-$Mes_2C_6H_3)_2$EP(O)C(IMe_4) but also the unsupported complexes (2,6-$Mes_2C_6H_3)_2$EPCO, which were fully characterized (E = Sb, Bi). This strategy proved useful for the preparation of the analogous group 13 compounds (2,6-$Mes_2C_6H_3)_2$EPCO (E = Ga, In).[5] The experimental work was augmented by DFT calculations, which provided PCO dissociation energies as well as relative energies of different PCO coordination. Electronic bond characteristics of the PCO fragment within its different chemical environments,

[a] D. Duvinage,[+] M. Janssen,[+] Dr. E. Lork, Prof. Dr. J. Beckmann
Institut für Anorganische Chemie und Kristallographie,
Universität Bremen, Leobener Straße 7,
28359 Bremen, Germany
E-mail: j.beckmann@uni-bremen.de
[b] Prof. Dr. H. Grützmacher
Laboratory of Inorganic Chemistry,
ETH Zürich, Vladimir-Prelog-Weg 1–5/10,
8093 Zürich, Switzerland
[c] Dr. S. Mebs
Institut für Experimentalphysik,
Freie Universität Berlin, Arnimallee 14,
14195 Berlin, Germany
E-mail: stefan.mebs@fu-berlin.de
[+] These authors contributed equally.

Supporting information for this article is available on the WWW under https://doi.org/10.1002/zaac.202200133

Journal of Inorganic and General Chemistry
ZAAC
Zeitschrift für anorganische und allgemeine Chemie

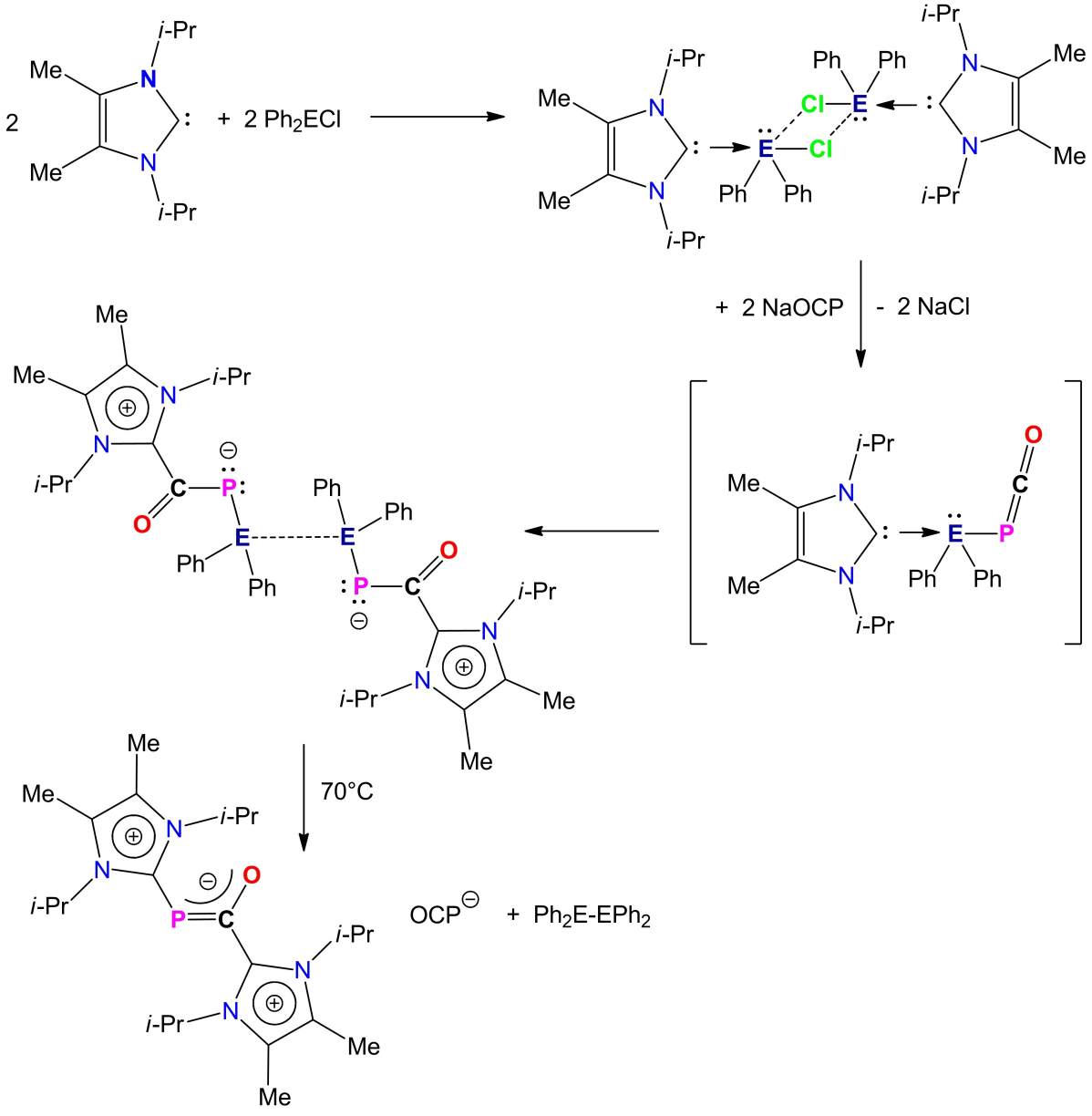

Scheme 1. Reaction of NHC-substituted heavier diphenylpnictogene chlorides with sodium phosphaethynolate according to Benkő and Gilliard et al.[4]

including the deconvolution of covalent and non-covalent bonding aspects, was provided by subsequent real-space bonding indicator (RSBI) analysis of the electron and electron pair densities.

Results and Discussion

Synthesis and Characterization

The reaction of the bis(*m*-terphenyl)element halides, (2,6-$Mes_2C_6H_3)_2SbCl$[6] and (2,6-$Mes_2C_6H_3)_2BiCl$[7] with [Na(1,4-dioxane)$_{2.5}$][PCO][3] afforded the bis(*m*-terphenyl)element phosphaethynolates, (2,6-$Mes_2C_6H_3)_2EPCO$ (**1**, E = Sb; **2**, E = Bi) as yellow and orange solids in yields of 80 and 86% (Scheme 2). The ^{31}P NMR spectra (C_6D_6) of **1** and **2** exhibit signals at –314.9 and –324.0 ppm are midway to those of the group 13 analogues (2,6-$Mes_2C_6H_3)_2GaPCO$ (–283.3 ppm) and (2,6-$Mes_2C_6H_3)_2InPCO$ (–336.2 ppm). The molecular structures of **1** and **2** are shown in Figure 1. For both compounds, the phosphaketene coordination mode applies. The Sb–P and Bi–P bond lengths of **1** (2.5479(8) Å) and **2** (2.655(3) Å) are in good agreement with sum of covalence radii (2.51 and 2.62 Å).[8] The M–P–C angles are almost rectangular and the P–C–O angle is nearly straight (M = Sb, Bi). The P–C bond lengths of **1** (1.655(4) Å) and **2** (1.67(2) Å) are larger than in the group 13

Journal of Inorganic and General Chemistry
ZAAC
Zeitschrift für anorganische und allgemeine Chemie

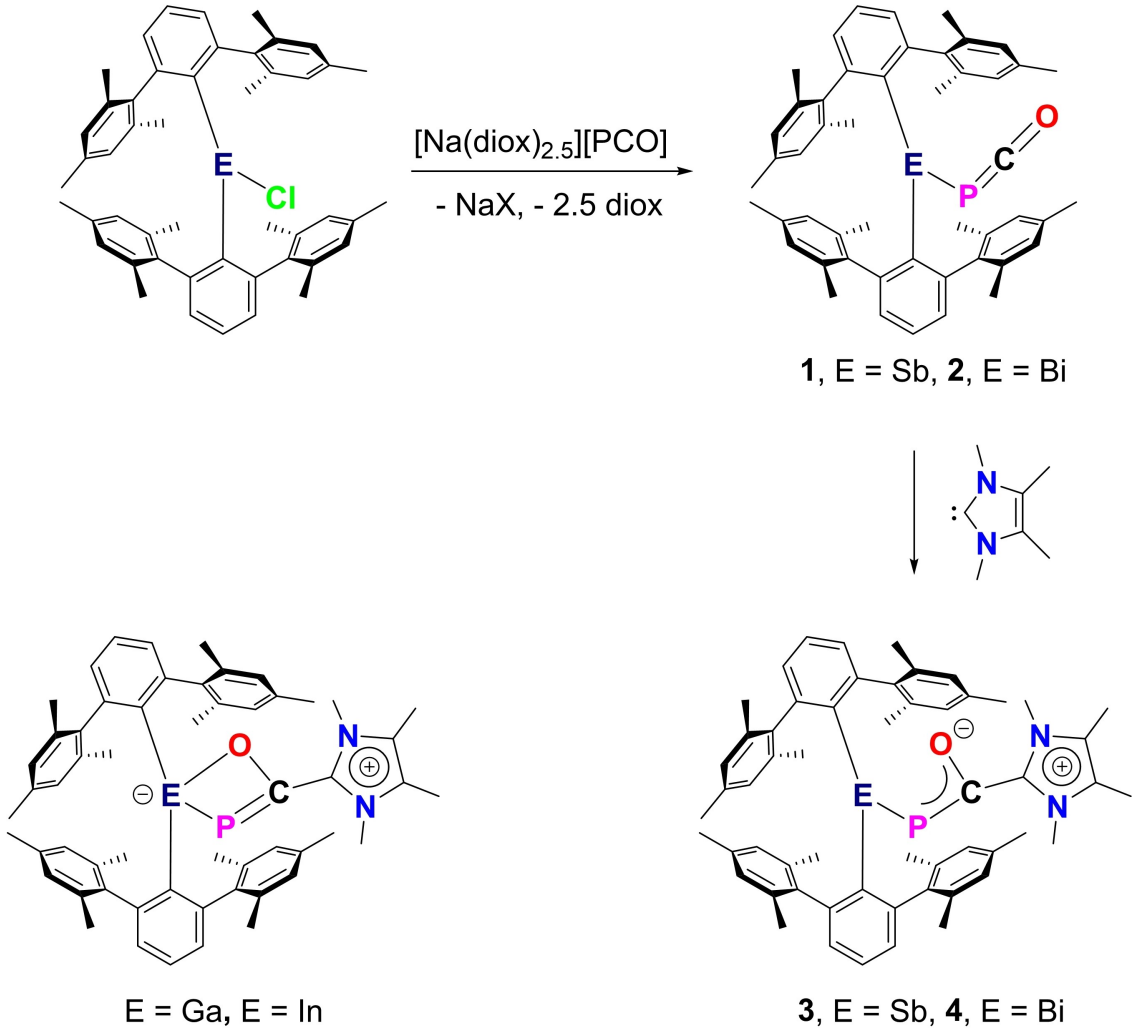

Scheme 2. Synthesis of **1**–**4**.

analogues (2,6-$Mes_2C_6H_3)_2$GaPCO (1.567(5) Å) and (2,6-$Mes_2C_6H_3)_2$InPCO (1.636(2) Å).[5] The C–O bond lengths of **1** (1.178(4) Å) and **2** (1.08(2) Å) as well as (2,6-$Mes_2C_6H_3)_2$GaPCO (1.224(5) Å) and (2,6-$Mes_2C_6H_3)_2$InPCO (1.174(2) Å) show a rather large variance, which is most likely an artifact of the crystal structure determination as (2,6-$Mes_2C_6H_3)_2EX_n$ structures often showing large vibrational displacement or disorder for the groups X. The asymmetric PCO stretching vibration of **1** (1920 cm^{-1}) and **2** (1901 cm^{-1}) are a more reliable parameter to evaluate the C–O bond, similar as in metal carbonyls.[9] Both parameters are slightly larger than in (2,6-$Mes_2C_6H_3)_2$GaPCO (1898 cm^{-1}) and (2,6-$Mes_2C_6H_3)_2$InPCO (1880 cm^{-1}). Judged by these values, the C–O bond strength most likely decreases for a series of (2,6-$Mes_2C_6H_3)_2$EPCO compounds in the order E = In > Ga > Bi > Sb. Additionally, for the evaluation of the C–P bond strength, the ^{13}C–^{31}P coupling constant in ^{13}C NMR spectroscopy, can be used. By the comparison of these, **1** ($^1J(^{13}C–^{31}P)$ = 113.9 Hz) and **2** ($^1J(^{13}C–^{31}P)$ = 114.8 Hz) show a much larger coupling constant than the group 13 homologs (2,6-$Mes_2C_6H_3)_2$GaPCO ($^1J(^{13}C–^{31}P)$ = 99.8 Hz) and (2,6-$Mes_2C_6H_3)_2$InPCO ($^1J(^{13}C–^{31}P)$ = 96.1 Hz), which proves that with decreasing C–O bond strength, the C–P bond strength increases in the order E = In < Ga < Sb ≤ Bi.

The reaction of **1** and **2** with 1,3,4,5-tetramethylimidazol-2-ylidene, IMe_4,[10] afforded the complexes (2,6-$Mes_2C_6H_3)_2$EP(O)C-(IMe_4) (**3**, E = Sb; **4**, E = Bi) as orange solids in 69 and 74% yield (Scheme 2). Interestingly, **4** is photo-sensitive in solution and even in the solid state when exposed to ambient light. During the course of days at room temperature, **4** decomposes into dibismuthene (2,6-$Mes_2C_6H_3Bi)_2$ and unaccounted decomposition products,[11] which suggest that migration of *m*-terphenyl substituents take place. In contrast, **3** is quite stable in solution and the solid state. The ^{31}P NMR spectra (C_6D_6) of **3** and **4** show signals at δ = 65.6 and 72.3 ppm, which are consistent with those of $Ph_2E(I^iPr_2Me_2)PCO$ (58.2 ppm for E = Sb and 82.2 ppm for E = Bi; $I^iPr_2Me_2$ = 1,3-diisopropyl-4,5-dimethylimidazol-2-ylidene),[4] but in marked difference to the ^{31}P NMR chemical shifts observed for (2,6-$Mes_2C_6H_3)_2$EP(O)C(IMe_4) (245.5 ppm for E = Ga and 219.7 ppm for E = In).[5] The different ^{31}P NMR chemical shifts are attributed to the bidentate coordination of

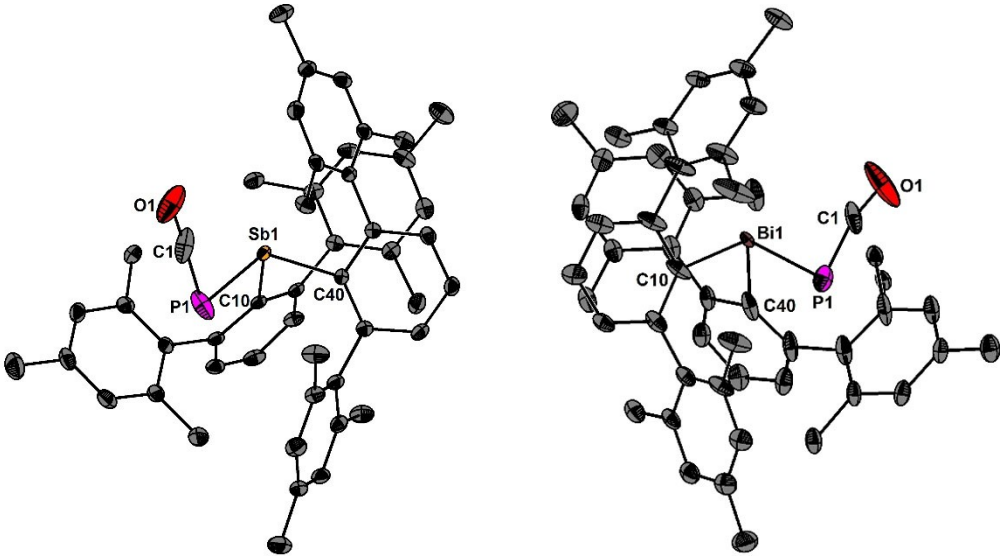

Figure 1. Molecular structures of **1** and **2** showing 50% probability ellipsoids and the essential numbering scheme. Selected bond parameters for **1** [Å, °]: Sb1-P1 2.5479(8), Sb1-C10 2.198(2), Sb1-C40 2.191(2), P1-C1 1.655(4), C1-O1 1.178(4), P1-Sb1-C10 101.68(6), P1-Sb1-C40 97.77(6), C10-Sb1-C40 103.94(8), C1-P1-Sb1 86.20(12), O1-C1-P1 176.7(3). Selected bond parameters for **2** [Å, °]: Bi1-P1 2.655(3), Bi1-C10 2.252(6), Bi1-C40 2.397(7), P1-C1 1.67(2), C1-O1 1.08(2), P1-Bi1-C10 91.6(2), P1-Bi1-C40 101.6(2), C10-Bi1-C40 103.7(2), C1-P1-Bi1 85.1(4), O1-C1-P1 166.1(1).

the PCO linkage (e.g. via P and O) in the group 13 compounds and the monodentate coordination of the PCO linkage (e.g. only via P) in the group 15 compounds (Scheme 2). The molecular structures of **3** and **4** are shown in Figure 2. The spatial arrangement of the Sb and Bi is tetrahedral taking into account the C_2P donor set and the electron lone pair. Repulsion of the latter presumably prevents a bidentate coordination mode. This observation is reminiscent to the bond situation in the zwitterionic diaryltelluronium acetimidate (8-$Me_2NC_{10}H_6)_2TeN(O)CH_3$, in which the lone pair at Te prevents

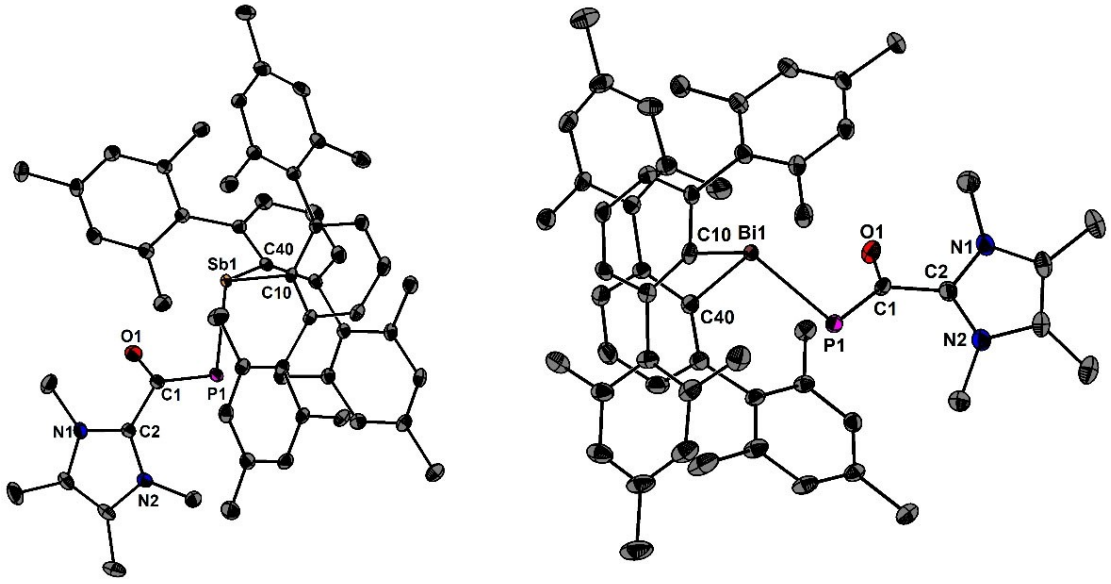

Figure 2. Molecular structures of **3** and **4** showing 50% probability ellipsoids and the essential numbering scheme. Selected bond parameters of **3** [Å, °]: Sb1-P1 2.4833(5), Sb1-C40 2.213(2), Sb1-C10 2.201(2), P1-C1 1.759(2), C1-O1 1.249(2), C1-C2 1.516(3), P1-Sb1-C10 105.17(5), P1-Sb1-C40 94.37(5), C10-Sb1-C40 100.13(7), O1-C1-P1 132.89(15). Selected bond parameters of **4** [Å, °]: Bi1-P1 2.605(2), Bi1-C10 2.329(4), Bi1-C40 2.361(4), P1-C1 1.753(6), C1-O1 1.263(7), C1-C2 1.518(7), P1-Bi1-C10 99.7(1), P1-Bi1-C40 108.7(1), C10-Bi1-C40 99.8(1), O1-C1-P1 129.4(4).

the coordination of the oxygen atom.[12] The Sb–P and Bi–P bond lengths of **3** (2.4833(5) Å) and **4** (2.605(2) Å) are slighter shorter than those of **1** and **2**. The C–C-bond lengths accounting for the coordination of the NHCs to the PCO moieties of **3** (1.516(3) Å) and **4** (1.518(7) Å) are consistent with values observed for $Ph_2E(I^iPr_2Me_2)PCO$ (1.529(7) Å for E = Sb and 1.515(1) Å for E = Bi; $I^iPr_2Me_2$ = 1,3-diisopropyl-4,5-dimethylimidazol-2-ylidene).[4] In contrast to **3** and **4**, the C–C bond lengths between the NHC moiety and the OCP unit in $(2,6\text{-}Mes_2C_6H_3)_2EP(O)C(IMe_4)$ (1.489(6) Å for E = Ga and 1.462(8) for E = In)[5] are shorter suggesting that this interaction is stronger in group 13 than in group 15 element compounds. No reaction of **3** or **4** with sulfur, selenium or tellurium was observed, which is another difference to the group 13 species.

Computational analysis

Efforts were made to obtain relaxed gas-phase geometries of the entire series of group 15 bis(*m*-terphenyl)element phosphaethynolates in the phosphaketene coordination mode $(2,6\text{-}Mes_2C_6H_3)_2EPCO$ as well as in the oxyphosphaalkyne coordination mode $(2,6\text{-}Mes_2C_6H_3)_2EOCP$ (E = N-Bi) by using density functional theory (DFT) calculations at the B3PW91/6-311 + G(2df,p) level of theory. For E = N–As, the phosphaketene coordination is energetically favored by 105–244 kJ mol^{-1} (Table S1) over oxyphosphaalkyne coordination. All attempts to optimize the oxyphosphaalkyne coordination mode for E = Sb, Bi lead to conversion into the phosphaketene coordination mode. The same trend was observed for the related series of compounds involving group 13 elements (B–Tl), although the energetic differences were considerably smaller.[5] Using the experimentally obtained structure of **3**, relaxed gas-phase geometries and energies were calculated for the whole series of $(2,6\text{-}Mes_2C_6H_3)_2EP(O)(IMe_4)$ (E=N–Bi). In all cases, except P, the monodentate coordination mode was confirmed. Only for E=P, the bidentate coordination mode reminiscent of the group 13 elements was found.[5] The electronic characteristics of the P–C and C–O bonds of the PCO ligand, and the E–P bonds (E = Sb, Bi) of 1–**4** were determined by a suitable set of real-space bonding indicator (RSBI) parameters for the gas-phase structures. RSBI comprise several complementary tools, such as the Atoms-In-Molecules (AIM)[13] bond topology, noncovalent interactions index (NCI)[14] derived intramolecular contact patches, as well as bonding and lone-pair basins using the electron localizability indicator (ELI-D).[15] Bond polarities are estimated by the Raub-Jansen Index (RJI),[16] which superimposes ELI-D (bonding) basins with the contributing adjacent AIM atoms, thus quantifying the electron density (ED, $\rho(\mathbf{r})$) distribution along a bond. Iso-surfaces of NCI and ELI-D show spatial complementary, suggesting at least partial spatial separation of covalent and non-covalent bonding aspects.[17–19] The combined use of AIM, NCI, and ELI-D provides a comprehensive picture of chemical bonds in real-space. For **1** and **3**, the topological and integrated AIM and ELI-D parameters are collected in Table 1 and the AIM topology as well as suitable NCI and ELI-D iso-surfaces are displayed in Figures 3 and 4 (for **2** and **4**, see Figures S17 and S18). For all bonds, d is the geometric contact distance, $\rho(\mathbf{r})_{bcp}$ is the electron density at the bcp, $\nabla^2\rho(\mathbf{r})_{bcp}$ is the corresponding Laplacian, ε is the bond ellipticity, $G/\rho(\mathbf{r})_{bcp}$ and $H/\rho(\mathbf{r})_{bcp}$ are the kinetic and total energy density over $\rho(\mathbf{r})_{bcp}$ ratios, N_{ELI} and V_{ELI} are electron populations and volumes of related ELI-D basins, γ_{ELI} is the ELI-D value at the attractor position, RJI is the Raub-Jansen Index. The E–P bond formation is visible in the AIM topology, and in addition numerous weak secondary interactions are found between the P atom and the organic ligands (Figures 3a, 4a S17a and S18a). For the C–O bond, strong covalent as well as strong ionic bond contributions are present. In terms of topological ED analysis at the bond critical point (bcp), this results in a strongly negative ratio of the total energy density and the ED ($H/\rho(\mathbf{r})_{bcp}$; covalent bonding aspects) and strongly positive ratio of the kinetic energy density and the ED ($G/\rho(\mathbf{r})_{bcp}$; ionic bonding aspects). Consequently, the Laplacian of the ED ($\nabla^2\rho(\mathbf{r})_{bcp}$) is close to zero

Table 1. Topological and integrated AIM and ELI-D properties of relevant interactions.

	contact or basin	d [Å]	$\rho(\mathbf{r})_{bcp}$ [eÅ^{-3}]	$\nabla^2\rho(\mathbf{r})_{bcp}$ [eÅ^{-5}]	ε	$G/\rho(\mathbf{r})_{bcp}$ [a.u.]	$H/(\mathbf{r})_{bcp}$ [a.u.]	N_{ELI} [e]	V_{ELI} [Å^3]	γ_{ELI}	RJI
$[PCO]^-$	C–O	1.195	2.90	−1.3	0.00	1.80	−1.83	2.18	2.3	1.49	80.8
1	C–O	1.160	3.14	5.9	0.01	2.01	−1.88	2.61	4.1	1.53	81.8
2	C–O	1.163	3.12	5.3	0.01	2.00	−1.88	2.57	3.9	1.53	81.7
3	C–O	1.245	2.64	−10.8	0.09	1.48	−1.76	1.93	2.1	1.55	76.2
4	C–O	1.246	2.63	−11.1	0.10	1.47	−1.76	1.93	2.1	1.55	76.1
3	C–C	1.495	1.76	−16.0	0.09	0.28	−0.92	2.52	6.1	1.97	66.3
4	C–C	1.495	1.76	−15.9	0.09	0.28	−0.92	2.51	6.0	1.97	66.3
$[PCO]^-$	P–C	1.619	1.22	13.7	0.00	1.67	−0.88	2.47	8.4	1.53	95.5
1	P–C	1.661	1.15	10.6	0.36	1.53	−0.88	3.17	10.7	1.67	93.1
2	P–C	1.657	1.16	11.0	0.33	1.54	−0.88	3.22	11.3	1.66	93.1
3	P–C	1.757	1.14	0.6	0.37	1.01	−0.97	2.59	6.7	1.79	86.0
4	P–C	1.755	1.14	0.8	0.36	1.02	−1.07	2.59	6.7	1.79	86.2
1	Sb–P	2.554	0.49	−0.2	0.02	0.35	−0.37	1.48	5.3	1.54	58.9
2	Bi–P	2.654	0.44	0.6	0.02	0.40	−0.31	1.10	4.0	1.52	61.9
3	Sb–P	2.493	0.57	−0.7	0.06	0.32	−0.41	1.82	6.8	1.56	55.3
4	Bi–P	2.594	0.51	0.1	0.07	0.37	−0.35	1.59	6.3	1.52	58.5

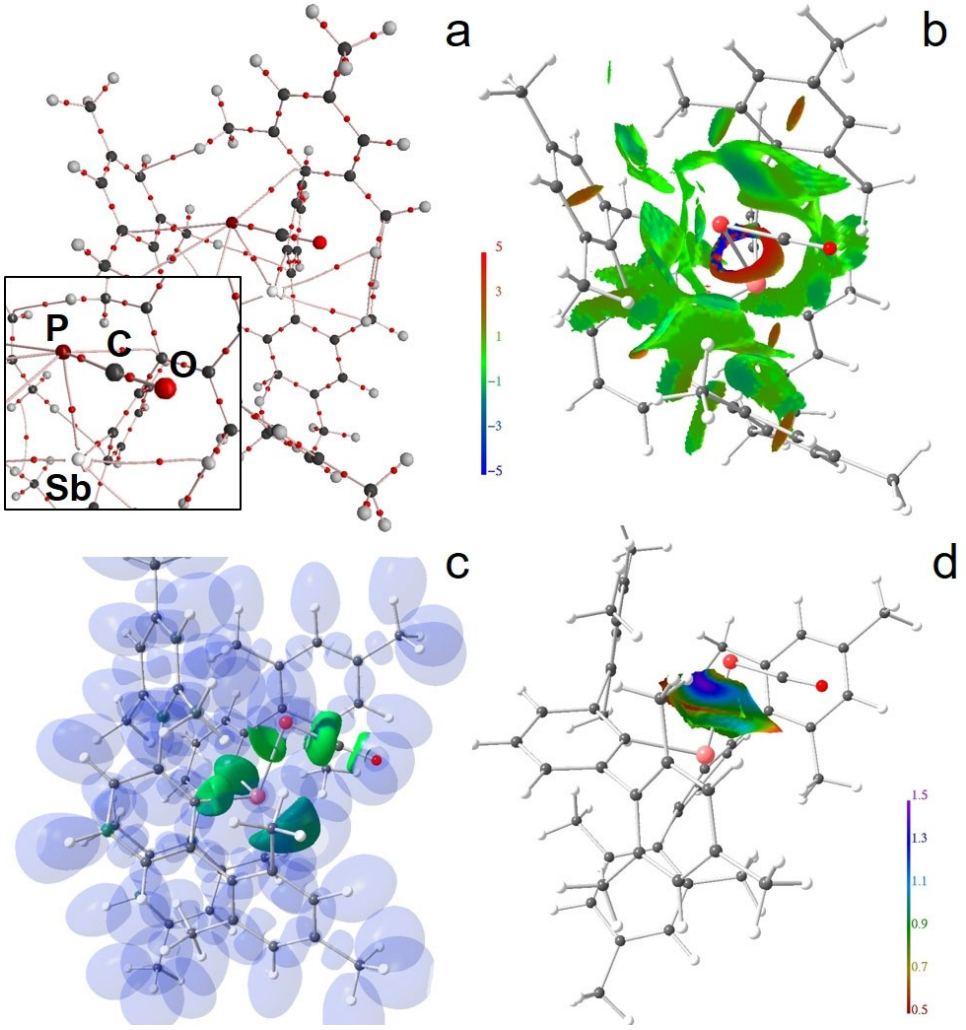

Figure 3. RSBI analysis of **1** (a) AIM bond paths motif, (b) NCI *iso*-surface at $s(\mathbf{r}) = 0.5$, (c) ELI-D localization domain representation at *iso*-value of 1.3, (d) ELI-D distribution mapped on the Sb–P ELI-D basin.

in the $[PCO]^-$ ion (in CO it is positive ($\nabla^2\rho(\mathbf{r})_{bcp} = 11$ eÅ^{-5}) because $G/\rho(\mathbf{r})_{bcp} = 2.17$ a.u. dominates over $H/\rho(\mathbf{r})_{bcp} = -1.94$ a.u.). The double-bond character of the C–O bond in PCO is reflected in a very large ED ($\rho(\mathbf{r})_{bcp} = 2.9$ eÅ^{-3}), compared to 3.4 eÅ^{-3} in free CO. With 81% the RJI bond polarity is between that obtained for covalent bonds (<70%) and ionic/dative bonds (>90%), i.e. about 80% of the ED within the C–O ELI-D bonding basin is located within the AIM basin of the C atom. Ionic bond contributions prevail in the P–C bond, which gives rise to a positive Laplacian ($|G/\rho(\mathbf{r})_{bcp}| > |H/\rho(\mathbf{r})_{bcp}|$; $\nabla^2\rho(\mathbf{r})_{bcp} = 14$ eÅ^{-5}) and a RJI of about 96%. The electronic characteristics of both bonds are only slightly affected by coordination to the $(2,6\text{-}Mes_2C_6H_4)_2E$ moiety: The C–O bond becomes a little shorter/stronger and the P–C bond becomes a little longer and weaker. In contrast, subsequent attachment of lMe_4 causes bending of the P–C–O axis and considerable bond elongation by about 0.09 Å (C–O) and 0.10 Å (P–C). Consequently, one finds decreased accumulations of the ED at the bcp in case of the C–O bond and inside the ELI-D bonding basin in both cases. For both bonds, the bond character changes towards higher relevance for covalent bonding aspects: $|H/\rho(\mathbf{r})_{bcp}| > |G/\rho(\mathbf{r})_{bcp}|$, RJI < 80% for C–O, and $|H/\rho(\mathbf{r})_{bcp}| \approx |G/\rho(\mathbf{r})_{bcp}|$, RJI < 90% for P–C, i.e. the changes exclusively go to the expense of ionic bonding aspects. The longer and weaker E–P bonds (E = Sb, Bi) become about 0.06 Å shorter *via* NHC coordination, however, with similar trends (diminished ionic bond contributions) in the electronic bond characteristics. Notably, in the group 13 series, they tend to become 0.02–0.04 Å longer.[5] In the NCI framework, thin ring-shaped basins enclose the E–P bond axes (E = Sb, Bi), pointing towards minor non-covalent bond contributions (Figures 3a, 4a S17a and S18a). In addition, numerous (extended) flat and greenish coloured basins are visible, uncovering a multitude of weak Van-der-Waals type interactions, some of which even give rise to the formation of a bcp in AIM topology, together transcending the Lewis picture of chemical bonding. The localization domain representation of the ELI-D shows that the E–P bonding basins stem from formerly non-bonding lone-pair basins of the P atom in **1** and **2**; at this *iso*-value ($\gamma = 1.3$) they are still topologically connected to the remaining lone-pair basins (Figures 3c, 4c S17c and

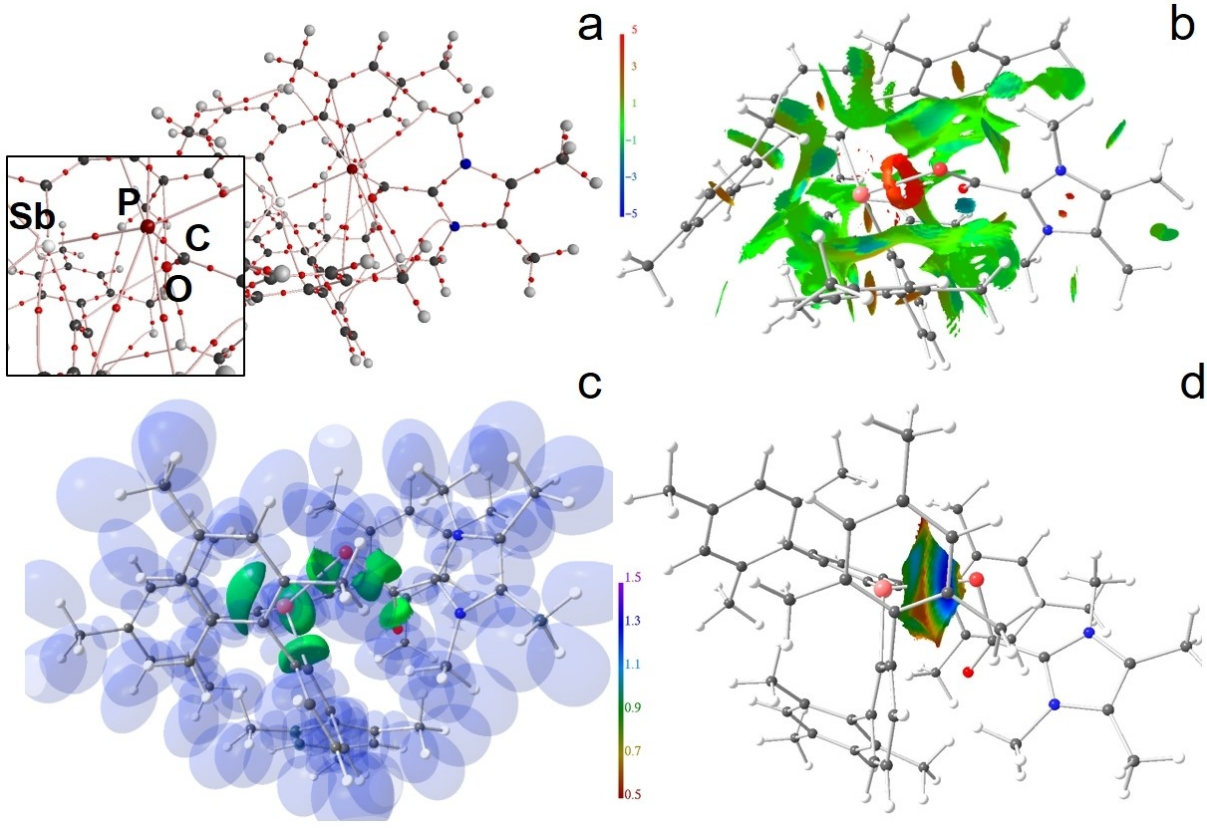

Figure 4. RSBI analysis of **3** (a) AIM bond paths motif, (b) NCI *iso*-surface at s(**r**) = 0.5, (c) ELI-D localization domain representation at *iso*-value of 1.3, (d) ELI-D distribution mapped on the Sb–P ELI-D basin.

S18c). The spatial requirements of the full E–P bonding basins is visible in Figures 3d, 4d S17d and S18d. Especially in **2**, the basin shape is almost flat in direction of the Bi atom, and only a shallow increase of electron localizability is visible, confirming the bond to be rather coordinative than dative, although these two terms are often used synonymously. AIM atomic and fragmental charges (Q_{AIM}) disclose effects of charge redistributions upon formation of **1**–**4**, whereby free CO and $[PCO]^-$ ion serve as reference (Table 2). Within the AIM framework, the strongly electronegative O and N atoms typically show strongly negative charges and vary only little in different chemical environments. It is thus not of surprise that Q_{AIM} for the O atoms vary only between −1.15 and −1.26 e in all compounds. Bearing this in mind, and comparing free CO with the free $[PCO]^-$ ion, the negative charge in the latter results in a situation in which the P and C atoms are *not* very positively charged, although being close to the O atom. Charge separation between the $(2,6\text{-}Mes_2C_6H_3)_2E]^+$ cation and PCO is less pronounced for Sb and Bi (about 0.3 e) than for Ga and In (about 0.5 e).[5] The hypothetical formation of **3** and **4** from $(2,6\text{-}Mes_2C_6H_3)_2E]^+$ and $[PCO]^-$ is accompanied by a charge transfer of about 0.7 e from the $[PCO]^-$ anion to the $(2,6\text{-}Mes_2C_6H_3)_2E]^+$ cation (E = Sb, Bi), which stem from the P atom (about 0.3 e), the C atom (about (0.3 e), and the O atom (about 0.1 e). This effect is partially inverted by addition of the IMe_4, which loses about 0.55 e in the process, bringing the atomic charges of the PCO moiety again closer to those found in the free $[PCO]^-$ ion.

Table 2. Atomic and fragmental AIM charges (in e).

	CO	$[PCO]^-$	**1**	**2**	**3**	**4**
E			1.04	1.00	0.94	0.91
R[a]			−0.36	−0.33	−0.39	−0.37
R′[a]			−0.37	−0.34	−0.40	−0.38
ERR′			0.31	0.33	0.15	0.16
P		0.19	0.46	0.48	0.20	0.21
C	1.20	0.07	0.39	0.36	0.33	0.32
O	−1.20	−1.26	−1.15	−1.16	−1.20	−1.20
PCO		−1.00	−0.30	−0.32	−0.67	−0.67
IMe_4					0.55	0.54
Σ	0.00	0.00	0.00	0.01	0.03	0.03

Conclusions

The kinetically stabilized diarylantimony and diarylbismuth phosphaethynolates $(2,6\text{-}Mes_2C_6H_3)_2EPCO$ (1, E = Sb; 2, E = Bi) were prepared and fully characterized. The stability of **1** and **2** is in marked contrast to the lighter congers Ph_2EPCO (E = Sb, Bi) that could not be isolated. The reaction of **1** and **2** with the small N-heterocyclic carbene (NHC), namely 1,3,4,5-tetramethylimidazol-2-ylidene (IMe_4) provided the complexes (2,6-

$Mes_2C_6H_3)_2EP(O)C(IMe_4)$ (**3**, E = Sb; **4**, E = Bi) that also show a higher thermal stability than $Ph_2E(I^iPr_2Me_2)PCO$ (E = Sb, Bi; $I^iPr_2Me_2$ = 1,3-diisopropyl-4,5-dimethylimidazol-2-ylidene).[4] In **3** and **4**, the coordination of the P(O)C(IMe_4) moiety occurs in a monodentate fashion (e.g. via P), whereas in the group 13 counterparts, (2,6-$Mes_2C_6H_3)_2EP(O)C(IMe_4)$ (E = Ga, In), the coordination is bidentate.[5] DFT quantified the energetic difference between different PCO coordination modes and found a significant preference for phosphaketene coordination; this preference is substantially larger than for the related group 13 compounds. Subsequent RSBI analysis indicated that – just like in CO – covalent and non-covalent (ionic) bonding aspects are equally relevant for the C–O bond in PCO^-, whereas ionic contributions prevail in the P–C bonds. Adduct formation with the IMe_4 moiety mainly goes to the expense of ionic bonding aspects in both bond types.

Experimental Section

General Information

All reactions and manipulations were performed under inert atmosphere (argon) using anhydrous solvents stored over 4 Å molecular sieves. Detailed general informations and synthetic aspects as well as NMR figures, UV-Vis figures and Computational and crystallographic details can be found in the supporting information. The NMR numbering scheme is different from the crystallographic numbering scheme. For details see the NMR figures in the supporting information.

Synthesis and characterization of (2,6-$Mes_2C_6H_3)_2SbPCO$ (1). (2,6-$Mes_2C_6H_3)_2SbCl$ (50.0 mg, 57.4 µmol, 1.00 eq.) and Na(1,4-dioxane)$_{2.5}$OCP (17.3 mg, 57.4 µmol, 1.00 eq.) were suspended in toluene (6 mL) and stirred for 18 hours, additionally the suspension is filtered and the solvent of the remaining solution is removed under vacuum to yield the target compound (2,6-$Mes_2C_6H_3)_2SbPCO$ as yellow solid (40.3 mg, 50.3 µmol, 83 %). Crystals suitable for X-Ray structure determination were grown from a hot toluene solution.

^{1}H NMR (600 MHz, C_6D_6): δ(ppm) = 6.99 (t, $^3J(^1H–^1H)$ = 7.51 Hz, 1H, H4), 6.76 (s, 2H, H9 or H11), 6.74 (s, 2H, H9 or H11), 6.72 (d, $^3J(^1H–^1H)$ = 7.52 Hz, 2H, H3 and H5), 2.18 (s, 6H, H14), 1.92 (s, 6H, H13), 1.82 (s, 6H, H15). **$^{13}C\{^1H\}$ NMR (151 MHz, C_6D_6)**: δ(ppm) = 193.58 (d, $^1J(^{13}C–^{31}P)$ = 113.88 Hz, C16), 150.48 (s, C2 and C6), 140.78 (s, C7), 140.66 (d, $^2J(^{13}C–^{31}P)$ = 7.57 Hz, C1), 137.73 (s, C12), 137.46 (s, C10), 137.31 (s, C8), 131.27 (s, C3 and C5), 129.32 (s, C9 and C11), 129.13 (s, C4), 22.64 (s, C13), 22.53 (s, C15), 21.04 (s, C14). **$^{31}P\{^1H\}$ NMR (243 MHz, C_6D_6)**: δ(ppm) = −314.94 (s). **HRMS ESI (m/z)**: No signal found in positive nor negative mode. **IR (ATR, neat)**: $\tilde{\nu}$ = 2915 (m), 1920 (s), 1610 (w), 1552 (w), 1435 (m), 1378 (w), 1180 (w), 1068 (w), 1034 (w), 909 (w), 847 (s), 802 (m), 760 (w), 736 (w), 695 (w), 657 (w) cm^{-1}. UV-Vis (Toluene, 10 µM) λ(abs) = 286, 344 nm. Melting point = 198 °C (decomp.).

Synthesis and characterization of (2,6-$Mes_2C_6H_3)_2BiPCO$ (2). (2,6-$Mes_2C_6H_3)_2BiCl$ (50.0 mg, 57.4 µmol, 1.00 eq.) and Na(1,4-dioxane)$_{2.5}$OCP (17.3 mg, 57.4 µmol, 1.00 eq.) were suspended in toluene (6 mL) and stirred for 18 hours, additionally the suspension is filtered and the solvent of the remaining solution is removed under vacuum to yield the target compound (2,6-$Mes_2C_6H_3)_2BiPCO$ as orange solid (40.3 mg, 50.3 µmol, 83 %). Crystals suitable for X-Ray structure determination were grown from a hot toluene solution.

^{1}H-NMR (600 MHz, C_6D_6): δ(ppm) = 7.04 (t, $^3J(^1H–^1H)$ = 7.39 Hz, 1H, H4), 6.94 (d, $^3J(^1H–^1H)$ = 7.43 Hz, 2H, H3 and H5), 6.81 (s, 4H, H9 and H11), 2.22 (s, 6H, H14), 1.98 (s, 6H, H13), 1.90 (s, 6H, H15). **$^{13}C\{^1H\}$ NMR (151 MHz, C_6D_6)**: δ(ppm) = 193.60 (d, $^1J(^{13}–)$ = 114.78 Hz, C16), 173.45 (s, C1), 150.71 (s, C2 and C6), 141.60 (s, C7), 137.30 (s, C12), 137.26 (s, C8), 136.75 (s, C10), 132.71 (s, C3 and C5), 129.32 (s, C9 and C11), 129.02 (s, C4), 22.45 (s, C13), 22.41 (s, C15), 21.20 (s, C14). **$^{31}P\{^1H\}$ NMR (243 MHz, C_6D_6)**: δ(ppm) = −324.04. **HRMS ESI (m/z)**: $[M+Cu]^+$ calculated. for $C_{49}H_{50}BiCuOP$*, 957.26938; found, 957.26769, $[M\text{-}CO+Cu]^+$ calculated for $C_{48}H_{50}BiCuP$, 929.27446; found, 929.27291, $[M\text{-}PCO]^+$ calculated. for $C_{48}H_{50}Bi$, 835.37110; found, 835.36947. **IR (ATR, neat)**: $\tilde{\nu}$ = 2915 (w), 1901 (s), 1610 (w), 1557 (w), 1435 (m), 1377 (w), 1179 (w), 1032 (w), 995 (w), 847 (s), 800 (m), 733 (m), 657 (w) cm^{-1}. UV-Vis (toluene, 10 µM) λ(abs) = 280, 352 nm. Melting point = 127 °C (decomp.).

* Measurement was repeated at different days. The Cu source is most likely the instrument.

Synthesis of (2,6-$Mes_2C_6H_3)_2SbP(O)C(IMe_4)$ (3). 1 (50.0 mg, 61.9 µmol, 1.00 eq.) and 1,3,4,5-tetramethylimidazol-2-ylidene (7.69 mg, 61.9 µmol, 1.00 eq.) were dissolved in THF (6 mL) and stirred for 24 hours. After filtration the solvent is removed under vacuum to yield the target compound ($Mes_2C_6H_3)_2SbP(O)C(IMe_4)$ (3) as yellow solid (40.0 mg, 42.9 µmol, 69 %). Crystals suitable for X-Ray structure determination were grown from a hot benzene solution.

^{1}H NMR (600 MHz, THF-d8): δ(ppm) = 7.11 (t, $^3J(^1H–^1H)$ = 7.46 Hz, 1H, H4), 6.59 (s (br), 4H, H9 and H11), 6.56 (d, $^3J(^1H–^1H)$ = 7.43 Hz, 2H, H3 and H5), 3.52 (s, 3H, H20 and H23), 2.22 (s (br), 6H, H14), 2.17 (s, 3H, H21 and H22), 1.76 (m, 12H). **$^{13}C\{^1H\}$ NMR (151 MHz, THF-d8)**: δ(ppm) = 198.53 (d, $^1J(^{13}C–^{31}P)$ = 81.55 Hz, C16), 152.34 (s, C2 and C6), 149.24 (d, $^2J(^{13}C–^{31}P)$ = 53.71 Hz, C17), 143.77 (s, (br), C7), 142.91 (d, $^2J(^{13}C–^{31}P)$ = 5.26 Hz, C1), 138.05 (s (br), C8 and C12), 136.07 (s (br), C10), 128.94 (s (br), C3 and C5), 128.02 (s, C9 and C11), 124.32 (s, C18 and C19), 33.35 (s, C20 or C23), 33.31 (s, C20 or C23), 23.52 (s (br), C13 and C15), 21.27 (s, C14), 8.33 (s, C21 and C22). **$^{31}P\{^1H\}$ NMR (243 MHz, THF-d8)**: δ(ppm) = 65.55. **HRMS ESI (m/z)**: $[M\text{-}PCO\text{-}NHC]^+$ calculated for $C_{48}H_{50}Sb$, 747.29452; found, 747.29452. **IR (ATR, neat)**: $\tilde{\nu}$ = 2915 (m), 2853 (m), 1771 (w), 1651 (w), 1610 (w), 1568 (w), 1505 (w), 1478 (m), 1435 (s), 1374 (s), 1261 (w), 1231 (w), 1177 (w), 1075 (w), 1032 (m), 928 (w), 847 (s), 801 (s), 735 (s), 680 (s) cm^{-1}. UV-Vis (toluene, 10 µM) λ(abs) = 288, 406 nm. Melting point = 126 °C (decomp.).

Synthesis of (2,6-$Mes_2C_6H_3)_2BiP(O)C(IMe_4)$ (4). 2 (50.0 mg, 55.9 µmol, 1.00 eq.) and 1,3,4,5-tetramethylimidazol-2-ylidene (6.94 mg, 55.9 µmol, 1.00 eq.) were dissolved in THF (6 mL) and stirred for 24 hours. After filtration the solvent is removed under vacuum to yield the target compound ($Mes_2C_6H_3)_2BiP(O)C(IMe_4)$ (4) as red solid (42.3 mg, 44.5 µmol, 74 %). Crystals suitable for X-Ray structure determination were grown from a hot benzene solution.

^{1}H NMR (600 MHz, C_6D_6): δ(ppm) = 7.19 (t, $^3J(^1H–^1H)$ = 7.44 Hz, 1H, H4), 6.98 (d, $^3J(^1H–^1H)$ = 7.44 Hz, 2H, H3 and H5), 6.84 (s, 2H, H9 or H11), 6.83 (s, 2H, H9 or H11), 3.16 (s, 3H, H20 and H23), 2.24 (s, 6H, H14), 2.12 (m, 12H, H13 and H15), 1.07 (s, 3H, H21 and H22). **$^{13}C\{^1H\}$ NMR (151 MHz, C_6D_6)**: δ(ppm) = 197.23 (d, $^1J(^{13}C–^{31}P)$ = 86.01 Hz, C16), 158.95 (s, C1), 152.37 (s, C2 and C6), 150.82 (d, $^2J(^{13}C–^{31}P)$ = 48.94 Hz, C17), 144.36 (s, C7), 137.74 (s, C8 or C12), 137.54 (s, C8 or C12), 135.47 (s, C10), 130.93 (s, C3 and C5), 128.74 (s, C9 and C11), 127.29 (s, C4), 122.31 (s, C18 and C19), 32.95 (s, C20 or C23), 32.91 (s, C20 or C23), 23.19 (s, C13 and C15), 21.26 (s, C14), 7.53 (s, C20 and C21). **$^{31}P\{^1H\}$ NMR (243 MHz, C_6D_6)**: δ(ppm) = 67.90. **HRMS ESI (m/z)**: $[M\text{-}PCO\text{-}NHC]^+$ calculated for $C_{48}H_{50}Bi$, 835.37110; found,

835.36947. **IR (ATR, neat)**: $\tilde{\nu}$ = 2914 (m), 1645 (w), 1563 (w), 1436 (s), 1371 (m), 1231 (w), 1176 (w), 1087 (w), 1031 (w), 1009 (w), 931 (w), 843 (s), 794 (s), 776 (w), 730 (s), 716 (w), 677 (m) cm^{-1}. UV-Vis (Toluene, 10 μM) λ(abs) = 305, 506 nm. melting point > 100 °C (decomp.).

Accession Codes

CCDC nos. 2127081–2127084 contain the supplementary crystallographic data for this paper. These data can be obtained free of charge from The Director, CCDC, 12 Union Road, Cambridge CB2 1EZ, UK (Fax: + 44-1223-336033; e-mail: deposit@ccdc.cam.ac.uk or http://www.ccdc.cam.ac.uk).

Acknowledgment

The Deutsche Forschungsgemeinschaft (DFG) is gratefully acknowledged for financial support. Open Access funding enabled and organized by Projekt DEAL.

Conflict of Interest

The authors declare no conflict of interest.

Data Availability Statement

The data that support the findings of this study are available from the corresponding author upon reasonable request.

Keywords: Antimony · Bismuth · Phosphaethynolate · Terphenyl · N-heterocyclic carbene

[1] J. M. Goicoechea, H. Grützmacher, *Angew. Chem. Int. Ed.* **2018**, *57*, 16968–16994; *Angew. Chem.* **2018**, *130*, 17214–17240.
[2] L. Weber, *Eur. J. Inorg. Chem.* **2018**, *20–21*, 2175–2227.
[3] R. E. Schreiber, J. M. Goicoecha, *Angew. Chem. Int. Ed.* **2021**, *60*, 3759–3767; *Angew. Chem.* **2021**, *133*, 3803–3811.
[4] J. E. Walley, E. Kertész, G. Wang, D. A. Dickie, Z. Benkő, R. J. Gillard, *Inorg. Chem.* **2021**, *60*, 4733–4743.
[5] D. Duvinage, M. Janssen, E. Lork, H. Grützmacher, S. Mebs, J. Beckmann, *Dalton Trans.* **2022**, ***51***, 7622–7629.
[6] M. Olaru, D. Duvinage, E. Lork, S. Mebs, J. Beckmann, *Angew. Chem. Int. Ed.* **2018**, *57*, 10080–10084; *Angew. Chem.* **2018**, *130*, 10237–10241.
[7] N. J. Hardman, B. Twamley, P. P. Power, *Angew. Chem. Int. Ed.* **2000**, *39*, 2771–2773; *Angew. Chem.* **2000**, *112*, 2884–2886.
[8] B. Cordero, V. Gómez, A. E. Platero-Prats, M. Revés, J. Echeverría, E. Cremades, F. Barragán, S. Alvarez, *Dalton Trans.* **2008**, 2832–2838.
[9] D. Heift, Z. Benkő, H. Grützmacher, *Dalton Trans.* **2014**, *43*, 5920–5928.
[10] A. J. Arduengo III, H. V. R. Dias, R. L. Harlow, M. Kline, *J. Am. Chem. Soc.* **1992**, *114*, 5530–5534.
[11] a) B. Twamley, C. D. Sofield, M. M. Olmstead, P. P. Power, *J. Am. Chem. Soc.* **1999**, *121*, 3357–3367; b) N. J. Hardman, B. Twamley, P. P. Power, *Angew. Chem. Int. Ed.* **2000**, *15*, 2771–2773.
[12] O. Mallow, J. Bolsinger, P. Finke, M. Hesse, Y.-S. Chen, A. Duthie, S. Grabowsky, P. Luger, S. Mebs, J. Beckmann, *J. Am. Chem. Soc.* **2014**, *136*, 10870–10873.
[13] R. W. F. Bader, *Atoms in Molecules: A Quantum Theory*, Cambridge University Press: Oxford U. K., **1991**.
[14] E. R. Johnson, S. Keinan, P. Mori-Sanchez, J. Contreras-García, A. J. Cohen, W. Yang, *J. Am. Chem. Soc.* **2010**, *132*, 6498–6506.
[15] M. Kohout, *Int. J. Quantum Chem.* **2004**, *97*, 651–658.
[16] S. Raub, G. Jansen, *Theor. Chem. Acc.* **2001**, *106*, 223–232.
[17] N. Gillet, R. Chaudret, J. Contreras-García, W. Yang, B. Silvi, J.-P. Piquemal, *J. Chem. Theory Comput.* **2012**, *8*, 3993–3997.
[18] P. de Silva, C. Corminboeuf, *J. Chem. Theory Comput.* **2014**, *10*, 3745–3756.
[19] S. Mebs, *Chem. Phys. Lett.* **2016**, *651*, 172–177.

Manuscript received: April 1, 2022
Revised manuscript received: June 7, 2022
Accepted manuscript online: June 13, 2022

